Check for updates

RESEARCH ARTICLE

NANO · MICRO small
www.small-journal.com

Unveiling Nanoscale Heterogeneity of Strain in $MAPbI_3$ Perovskite Films Using Bragg Coherent X-Ray Diffraction Imaging

*Dong Liang, Zhengtong Yao, Jiecheng Diao, Peng Li, Yuting Xiong, Xiaobin Xu, Ian Robinson, and Bo Chen**

Cation alloying and substrate morphology control have proved to be effective in controlling strains in perovskite films by macroscale characterizations. However, the nanoscale characterizations of strains are still limited, which hinder the comprehensive understanding of the strain regulation. Here, the strain regulation of $MAPbI_3$ ($MA = CH_3NH_2$) is done by Cs (Cesium) alloying and introduction of a nano-structured substrate to the perovskite films. Laboratory X-ray diffraction analysis shows that Cs alloying introduces compressive strain, whereas providing a nano-structured substrate introduces tensile strain. Bragg coherent X-ray diffraction imaging further demonstrates that nanoscale homogeneity of the strain in pure $MAPbI_3$ would be destroyed through 3 at% Cs alloying, as the strain varies from compressive to tensile. Both compressive and tensile domains exist in the perovskite crystals at the same time. The application of a nano-structured substrate is found to cause the nanoscale heterogeneity of strains in the $MAPbI_3$ films. The strain homogeneity caused by combining both 3% Cs alloying and providing a nano-structured substrate is found to enhance the structural stability of perovskite films. The results provide 3D nanoscale monitoring of strains for the purpose of strain regulation, which contributes to further understanding of the strains in perovskite materials.

1. Introduction

Halide perovskite materials are promising materials in photoelectric applications.[1] Their chemical formula is ABX_3, in which A and B represent cations and X represents halide. Due to their suitable bandgap, excellent carrier mobility, and long carrier lifetime, perovskite materials are widely used in various photoelectric devices, such as photodetectors,[2] light-emitting diodes,[3] and solar cells.[4] In the past decade, the power conversion efficiency of perovskite solar cells (PSCs) has rocketed from 3.8%[5] to 26.1%,[6] making it possible to replace silicon (Si) cells in the photovoltaic field. Perovskite materials are thus considered to be the most promising candidates for the next generation of designable, low-cost, and high-efficient solar cells.[7]

The structural strain in perovskite materials has been shown to be influential to their photoelectrical performance.[8] For commonly used perovskite films, strain primarily arises from the internal nonperiodicity of the crystal lattice,[9] and the mismatch of the thermal expansion coefficients between the perovskite film and its substrate.[10] Residual strain can influence various properties of perovskite films, such as bandgap, carrier transport, defect characteristics, nonradiative recombination, and structural stability, thereby affecting the optoelectronic performance of PSCs.[11] Various methods have been applied to regulate the strain of perovskite

D. Liang, Z. Yao, Y. Xiong, X. Xu, B. Chen
School of Materials Science and Engineering
Tongji University
Shanghai 201804, China
E-mail: bo.chen@tongji.edu.cn

D. Liang, B. Chen
Key Laboratory of Advanced Civil Engineering Materials of the Ministry of Education
Tongji University
Shanghai 201804, China

J. Diao
Center for Transformative Science
ShanghaiTech University
Shanghai 201210, China

P. Li
National Synchrotron Radiation Laboratory and School of Nuclear Science and Technology
University of Science and Technology of China
Hefei 230029, China

P. Li
Diamond Light Source
Harwell Science and Innovation Campus
Didcot OX11 0DE, UK

I. Robinson
London Centre for Nanotechnology
University College London
London WC1H 0AH, UK

The ORCID identification number(s) for the author(s) of this article can be found under https://doi.org/10.1002/smll.202501920

DOI: 10.1002/smll.202501920

 © 2025 Wiley-VCH GmbH

films, often known as strain engineering, of which cation alloying and substrate morphology control are the two most important ones.[12] Cation alloying introduces cations with different sizes, such as Cs^+ (Cesium ion), MA^+ ($MA = CH_3NH_2$), and FA^+ ($FA = NHCHNH_2$) to regulate strain.[13] Substrate morphology control, on the other hand, manipulates the interface between the substrate and the perovskite film. The effectiveness of strain regulation can be evaluated by X-ray diffraction (XRD) monitoring.[14] However, XRD can only characterize the strain field in average on the macroscale. It lacks the ability to probe the local strain variation at nanoscale.[15] In fact, the strain in most perovskite films is not homogeneously distributed, forming heterogeneous strained areas ranging from a few nanometers to hundreds of micrometers.[16] The nanoscale characterizations of strain fields would contribute to the comprehensive understanding of strain regulation mechanisms. Besides, such nanoscale characterization can promote the understanding of how strain affects the photoelectric performance and long-term stability of perovskite and their devices.

Bragg coherent X-ray diffraction imaging (BCDI), a strain-sensitive measurement tool, can image the individual crystal shape in 3D and map out the strain distribution inside the whole crystal grain with nanometer spatial resolution.[17] By illuminating the sample with a coherent X-ray beam, the diffraction patterns at certain Bragg angles could be recorded, which include extra interference fringes. For data acquisition, a series of diffraction pattern slices are recorded by making a small rotation of the sample around the selected Bragg peak. The detector can only record the intensity, but not the phase information about the diffraction signal, causing the famous "phase problem". To address this, iterative phase retrieval algorithms are used to reconstruct the 3D electron density function $\boldsymbol{\rho(r)}$ of the sample in BCDI.[18] Generally, $\boldsymbol{\rho(r)}$ is a complex function consisting of amplitude and phase. The amplitude is proportional to the crystal's electron density function. The phase is proportional to the atomic displacement along the direction of the X-ray scattering vector (**Q**). As the strain due to atomic displacements breaks the symmetry of the Bragg diffraction patterns, BCDI can be utilized to quantitatively analyze strain at nanoscale. This method has been applied to track the volume change of silver (Ag) single crystals during electrochemical reactions,[19] the evolution of dislocation in lithium-rich layered oxides,[20] and the movement of dislocation in $MAPbBr_3$ film[21] for example.

In this study, the controllable regulation of strain in $MAPbI_3$ perovskite films was achieved by Cs alloying and by using a nanostructured substrate with nanocolumns on its surface, called a "nano-substrate". The Cs alloying introduced compressive strain up to a maximum of −1.19% (absolute value). Nano-substrates, on the other hand, introduced tensile strain of 0.27% in $MAPbI_3$ films. Thereby variable Cs^+ compositions of films on a nano-substrate can be used to tune the average strain from positive to negative. The individual $MAPbI_3$ crystals were imaged in 3D by using BCDI, and heterogeneity of strain within the crystals was visualized, where it was found that the homogeneity of strain of the crystals can be destroyed with higher than 3 at% Cs alloying. The impact of strain on the stability against the decomposition of $MAPbI_3$ films was also studied, where the homogeneity of strain was found to increase structural stability and inhibit decomposition. Additionally, compressive strain via Cs alloying was found to help increase the intensity of infrared absorption due to the compact lattice. This research provides the direct strain information in perovskite films at nanoscale, and is expected to support the future application of strain engineering to the PSCs.

2. Results and Discussion

2.1. Chemical Components and Surface Morphology

The XRD and scanning electron microscopy (SEM) results are shown in **Figure 1**. In the lab XRD patterns, three peaks are located at 13.96°, 28.29°, and 31.73°, corresponding to (110), (220), and (310) planes of tetragonal $MAPbI_3$, respectively (Figure 1a,b).[22] The XRD patterns indicate good crystallinity of the $MAPbI_3$ films, which makes them suitable for BCDI. The peak located at 33° corresponds to the (200) Bragg reflection of the Si substrates (Figure S1, Supporting Information), which is due to the X-ray penetrating the perovskite film. This peak is the basis-forbidden reflection that is often shown in the XRD patterns of Si(100) wafers (as substrates).[23] The Si substrates used in this study were cut from single crystal Si wafers (100 mm diameter, single-side polished), which are P-type doping (boron doping) and with orientation of (100). The XRD results of Si substrates used in this study have been reported by Xiong et al. as well.[24] The peak located at 12.5° in the lab XRD patterns corresponds to the (001) plane of PbI_2 (Figure 1a,b, black arrow pointed). The appeared PbI_2 in the films is the product of $MAPbI_3$ decomposition, indicating the instability of $MAPbI_3$. For the samples prepared on flat-substrates, as the Cs contents increase from 0% to 7%, the peak heights of PbI_2 decrease (Figure 1c). As the Cs contents increase from 3% to 7%, the integral areas of PbI_2 peaks reduce (Figure 1d), indicating the reduction of PbI_2 contents. The decrease of peak heights and the integral areas with Cs alloying is also found in the XRD patterns of the samples prepared on nano-substrates (Figure 1e,f). This suggests that the Cs alloying can enhance the stability of $MAPbI_3$ and inhibit the decomposition.

The SEM images of perovskite films prepared on flat-substrates (Figure 1g–k) show that the films present good crystallinity with distinct grain shapes. The grain size ranges from 200 to 300 nm. Sheets are found on the surface of pristine $MAPbI_3$ film (Figure 1g), which are confirmed to be the PbI_2 according to the energy dispersive spectroscopy (EDS) results (Figure S2 and Table S1, Supporting Information). It indicates that the $MAPbI_3$ decomposes into PbI_2 due to its instability. After 1% Cs alloying, the number and size of PbI_2 on the surface both decrease (Figure 1h). As the Cs content increases further to 7%, PbI_2 nearly disappears and the flatness of films increases (Figure 1k). The SEM results support that Cs alloying can enhance the stability of perovskite films and inhibit their decomposition. The PbI_2 sheets on the films prepared on nano-substrates distribute mainly in the protruding areas, where the nanocolumns are located. It can be inferred that the nanocolumns cause a lattice mismatch between the perovskite film and the substrate. The lattice mismatch introduces stress and defects, thus accelerating the decomposition.

© 2025 Wiley-VCH GmbH

16136829, 0, Downloaded from https://onlinelibrary.wiley.com/doi/10.1002/smll.202501920 by Bo Chen - Tongji University , Wiley Online Library on [23/06/2025]. See the Terms and Conditions (https://onlinelibrary.wiley.com/terms-and-conditions) on Wiley Online Library for rules of use; OA articles are governed by the applicable Creative Commons License

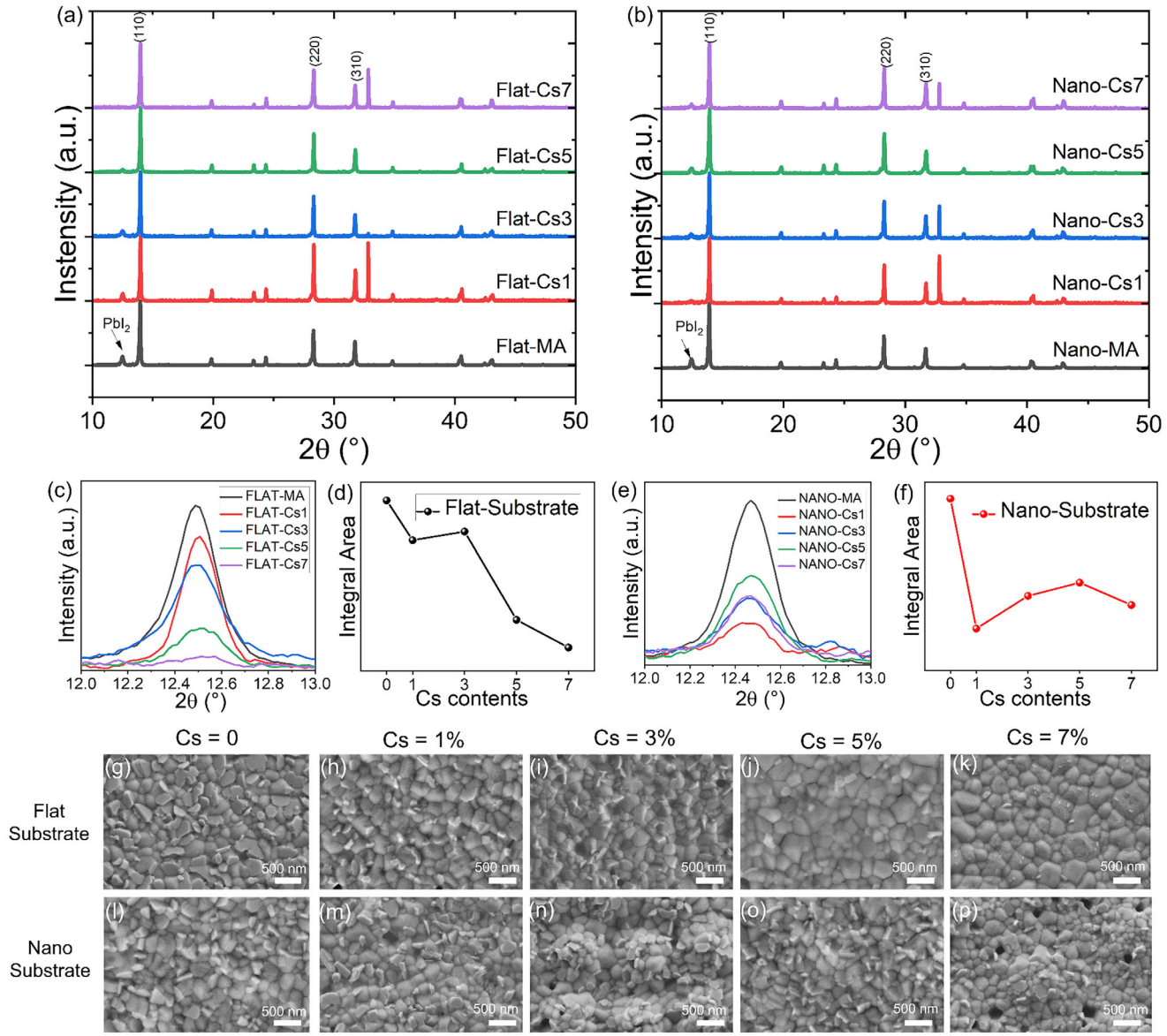

Figure 1. The chemical components and surface morphologies of the $MAPbI_3$ perovskite films. XRD patterns of the perovskite films on a) flat-substrates and b) nano-substrates. c) Details of the PbI_2 XRD peaks in panel (a). d) The integral areas of PbI_2 peaks in panel (a). e) Details of the PbI_2 XRD peaks in panel (b). f) The integral areas of PbI_2 peaks in panel (b). SEM images of the perovskite films on flat-substrates g) without Cs alloying, h) with 1% Cs alloying, i) with 3% Cs alloying, j) with 5% Cs alloying, and k) with 7% Cs alloying. SEM images of the perovskite films on nano-substrates l) without Cs alloying, m) with 1% Cs alloying, n) with 3% Cs alloying, o) with 5% Cs alloying, and p) with 7% Cs alloying.

2.2. Average Strain

The experimentally determined average strain in the perovskite films was obtained from the XRD patterns in Figure 1 on both flat- and nano-substrates and it is shown in **Figure** 2a. These calculations were done by measuring the difference of the interplanar spacing of the (110) plane ($d_{(110)}$) obtained by the Bragg's law. The calculation is as follows

$$\epsilon = \frac{d - d_0}{d_0} \quad (1)$$

where ϵ is the relative value of strain, d is the $d_{(110)}$ of the Cs alloyed perovskite samples, d_0 is the $d_{(110)}$ of pristine non-Cs alloyed $MAPbI_3$. Positive ϵ represents for tensile strain and negative ϵ represents for compressive strain.

After Cs alloying, compressive strains are found in the perovskite films on both flat- and nano-substrates. As the Cs content increases from 0% to 7%, the absolute value of compressive strain continuously increases. When the Cs content reaches 7%, the value of strain in film is −0.99% in flat-substrated sample and −1.19% in nano-substrated sample, respectively (Figure 2a). Tensile strain is usually introduced into the perovskite films by differential thermal contraction from an assumed strain-free epitaxy

© 2025 Wiley-VCH GmbH

16136829, 0, Downloaded from https://onlinelibrary.wiley.com/doi/10.1002/smll.202501920 by Bo Chen - Tongji University , Wiley Online Library on [23/06/2025]. See the Terms and Conditions (https://onlinelibrary.wiley.com/terms-and-conditions) on Wiley Online Library for rules of use; OA articles are governed by the applicable Creative Commons License

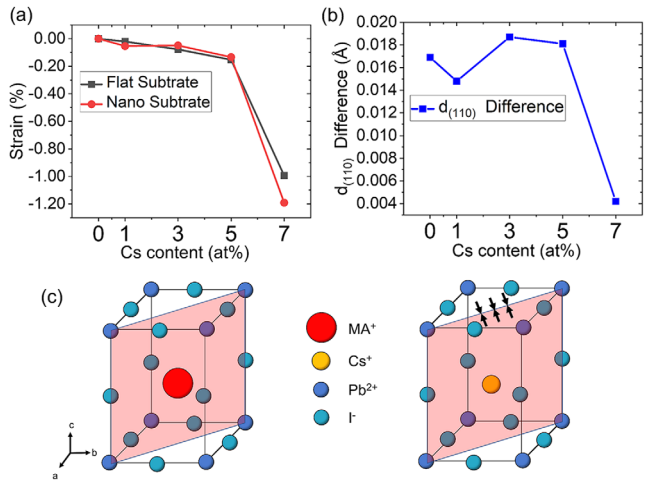

Figure 2. The strain of perovskite films. a) Average strain in perovskite films on flat- and nano-substrates, b) the difference of $d_{(110)}$ between the perovskite films on flat-substrates and the perovskite films on nano-substrates at the same Cs contents. c) Schematic diagram of Cs alloying regulating strain.

at the growth temperature. The strain can be estimated from the mismatch of the thermal expansion coefficient between the perovskite film (6.1×10^{-5} K^{-1} for $MAPbI_3$ film) and the substrate (2.6×10^{-6} K^{-1} for Si substrate).[14,25] Cs alloying, on the other hand, can introduce compressive strain to compensate the tensile strain, causing strain relaxation and even compressive strain in perovskite films. The schematic diagram of Cs alloying on regulating strain is shown in Figure 2c. Cs^+ has a smaller ion radius (164 pm) than that of the MA^+ (217 pm).[26] After Cs^+ occupies the A site (the center of the cubes in Figure 2c),$[PbI_6]^{4-}$ octahedral voids will generate more space. Therefore, Pb^{2+} and I^- will spontaneously approach Cs^+, manifested by the contraction of $[PbI_6]^{4-}$ octahedra toward Cs^+. In the (110) direction (the red plane in Figure 2c), the arrangement of atoms becomes more compact, resulting in a decrease in the $d_{(110)}$ and the introduction of compressive strain.

For non-Cs alloyed $MAPbI_3$ films, the $d_{(110)}$ difference is 0.017 Å (Figure 2b) and the calculated strain is 0.27% (dividing the $d_{(110)}$ difference by $d_{(110)\text{-Nano}}$ and taking a percentage). It indicates that nano-substrates introduce tensile strain in non-Cs alloyed $MAPbI_3$ films. The $d_{(110)}$ difference reaches a maximum of 0.019 Å in 3% Cs alloyed perovskite film on the nano-substrate and a minimum of 0.004 Å in 7% Cs alloyed perovskite film on the nano-substrate (Figure 2b). **Table 1** lists the $d_{(110)}$ of the perovskite films, where the last column gives the $d_{(110)}$ difference by subtracting the 4th column from the 2nd column. At the same Cs content, the $d_{(110)}$ of perovskite films on the nano-substrate are higher than that of on the flat-substrate. Specifically, $d_{(110)}$ of pristine $MAPbI_3$ film without Cs alloying on the nano-substrate is 0.017 Å higher than that of the film on the flat-substrate, 0.015 Å larger when 1% Cs alloying, 0.019 Å larger when 3% Cs alloying, 0.018 Å larger when 5% Cs alloying, and 0.004 Å larger when 7% Cs alloying. These differences of the $d_{(110)}$ at the same Cs contents suggest that nano-substrate can broaden the lattice of perovskite films due to the nanocolumns, resulting in the introduction of tensile strain. The morphology and quality of perovskite films are strongly related to the textures of the substrates.[27] The morphology of the nanocolumns on nano-substrates is shown in Figure S3 in the Supporting Information. When the perovskite crystals grow, the nanocolumns will apply constraints, which would cause lattice expansion of the perovskite films due to the protrusions, resulting in tensile strain in the perovskite films. Due to the presence of protruding nanocolumns array on the nano-substrates and the flexibility of the perovskite materials, the perovskite films prepared on nano-substrates have curved surfaces with multiple protrusions. In the nanocolumn region, during the crystal growth, the perovskite film is bent and exhibits a convex dome-shaped structure, where the surface of the film is stretched and thereby generating tensile strain in the film. Such physically introduced strain has been applied in the strain engineering of perovskite films.[16a,28]

2.3. Nanoscale Heterogeneity of Strain Distribution via BCDI Measurements

The reconstruction of the atomic displacements generated from the measured strain (from BCDI measurements) of the whole pristine $MAPbI_3$ crystal without Cs alloying on flat-substrate is shown in **Figure 3**a–d. For all the samples, the low errors (χ^2 values) show good reconstructions of the crystals (Figure S4 and Table S2, Supporting Information). The black arrows with letter "Q" in Figure 3 and **Figure 4** are the **Q** vectors, and the crystals are rendered in blue-to-red color. The color bar shows the atomic displacement from −2.11 to 2.11 Å along the **Q** direction. The crystal without Cs alloying is a grain with a length of about 200 nm and a thickness of 80 nm, which is consistent with the SEM images. The displacement variation is narrowly distributed between 0.44 and 1.14 Å across the entire crystal. No negative displacement being found indicates that no strain deviation from compressive strain to tensile strain (Figure S5a, Supporting Information). The strain in pristine $MAPbI_3$ without Cs alloying exhibits nanoscale

Table 1. $d_{(110)}$ of perovskite films.

Nano-substrated sample	$d_{(110)\text{-Nano}}$ [Å]	Flat-substrated sample	$d_{(110)\text{-Flat}}$ [Å]	$d_{(110)}$ difference[a)] [Å]
Nano-MA	6.355	Flat-MA	6.338	0.017
Nano-Cs1	6.351	Flat-Cs1	6.336	0.015
Nano-Cs3	6.352	Flat-Cs3	6.333	0.019
Nano-Cs5	6.346	Flat-Cs5	6.328	0.018
Nano-Cs7	6.279	Flat-Cs7	6.275	0.004

[a)] $d_{(110)}$ differences were obtained by subtracting $d_{(110)\text{-Flat}}$ from $d_{(110)\text{-Nano}}$

© 2025 Wiley-VCH GmbH

16136829, 0, Downloaded from https://onlinelibrary.wiley.com/doi/10.1002/smll.202501920 by Bo Chen - Tongji University , Wiley Online Library on [23/06/2025]. See the Terms and Conditions (https://onlinelibrary.wiley.com/terms-and-conditions) on Wiley Online Library for rules of use; OA articles are governed by the applicable Creative Commons License

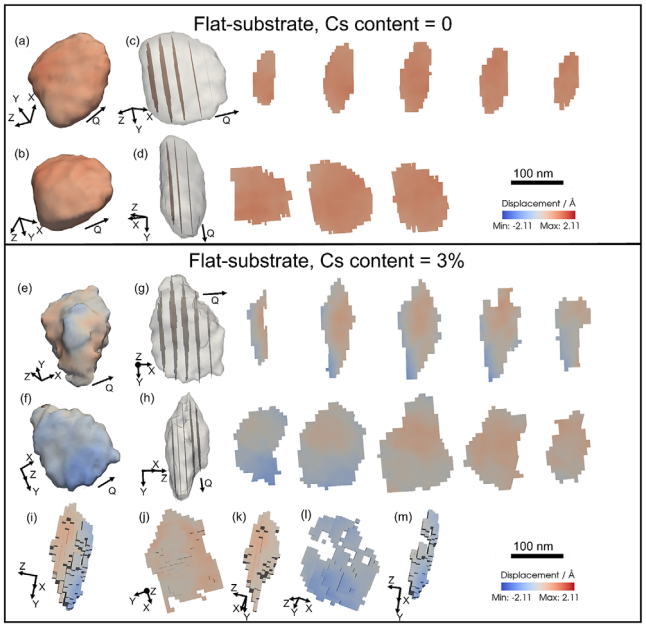

Figure 3. BCDI reconstructions of the perovskite crystals prepared on the flat-substrates. Panels (a) to (d) are from the same crystal reconstruction but along different orientations. a,b) The reconstructed $MAPbI_3$ crystal without Cs alloying from two different views. The atomic displacements within slices through the $MAPbI_3$ crystal (transparent objects), whose normal direction is c) along the **Q** direction and d) perpendicular to the **Q** direction. Panels (e) to (i) are from the same crystal reconstruction but along different orientations. e,f) The reconstructed 3% Cs alloyed perovskite crystal from two different views. The atomic displacements within slices through the 3% Cs alloyed perovskite crystal (transparent objects), whose normal direction is g) along the **Q** direction and h) perpendicular to the **Q** direction. i) Tensile and compressive domains in the 3% Cs alloyed perovskite crystal. The separated tensile domain from panel (i): j) the front view of the tensile domain and k) the side view of the tensile domain. The separated compressive domain from panel (i): l) the front view of the compressive domain and m) the side view of the compressive domain.

homogeneity of strain. After 1% Cs alloying, no negative displacement was found, which suggests that the sample remains homogeneity of strain in the perovskite crystal too (Figures S6 and S7, Supporting Information).

BCDI reconstruction of typical crystals in the perovskite film after 3% Cs alloying are shown in Figure 3e–m. The measured crystal in this sample is a grain with a size of 213 nm (Figure 3e,f). The histogram of the displacement distribution in this crystal is shown in Figure S5b in the Supporting Information. Both tensile strain with a displacement maximum of 0.62 Å (Figure 3e) and compressive strain with a displacement maximum (absolute value) of −0.99 Å (Figure 3f) are found on the crystal surface, indicating the heterogeneity of strain. In the slice images along the **Q** direction (Figure 3g), the displacement shifts from negative (blue) to positive (red) from the outer side to the inner side of the crystal, which indicates the deviation of strain from compressive strain to tensile strain. In the 2nd and 3rd slices in Figure 3g, the displacement field manifests as a radical area with a maximum displacement of 0.62 Å, suggesting that there is a tensile strain core. The displacement decreases as it moves away from the center, indicating the relaxing tensile strain. Moreover, two domains in the crystal are discovered, as known as the tensile domain and compressive domain, respectively (Figure 3i–m). Both the tensile domain and the compressive domain are sheet-shaped and they stick together face to face. The volume fraction of the tensile domain is 1.5 times as large as that of the compressive domain (**Table 2**). The average displacement in the tensile domain is 0.24 Å and the average displacement in the compressive domain is −0.28 Å (Table 2). This deviation of strain is the result of component segregation that can be seen in BCDI results.[29] It can be inferred that by 3% Cs alloying, the segregated Cs^+ in the perovskite crystal causes the deviation of strain.

The reconstructed 3D images of $MAPbI_3$ crystal without Cs alloying on nano-substrate are shown in Figure 4a–d. Figure 4a,b presents the same 3D images of the sample from different orientations. The histogram of the displacement distribution in this crystal is shown in Figure S8a in the Supporting Information. It can be seen that the atomic displacement in the $MAPbI_3$ crystal on the nano-substrate shifts from negative (blue area in Figure 4a) to positive (red area in Figure 4b) from one side to the other, indicating the change of strain. Such shifts can be further presented through the slice images of the crystal (Figure 4c,d). Along the **Q** direction, the 1st slice in Figure 4c shows a positive strained area (with red color) with 0.84 Å displacement. Then, a neutral strained area (with gray color) with an average displacement of 0.02 Å appears, and it enlarges, which can be seen from the 2nd to 4th slice in Figure 4c. In the 5th slice in Figure 4c, a negative strained area (with blue color) is found where

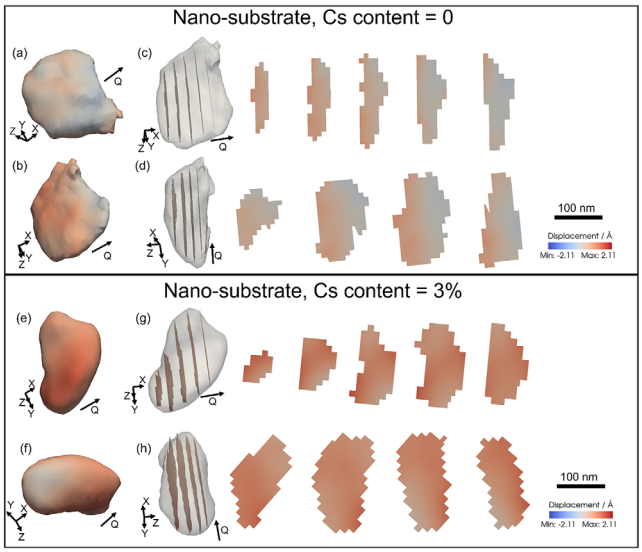

Figure 4. BCDI reconstruction of perovskite crystals grown on the nano-substrates. Panels (a) to (d) present the same crystal reconstruction but along different orientations. a,b) The reconstructed 3D views of $MAPbI_3$ crystal grown on the nano-substrate. The atomic displacements within slices through the $MAPbI_3$ crystal (transparent objects), whose normal direction is c) along the **Q** direction and d) perpendicular to the **Q** direction. Panels (e) to (h) present the same crystal reconstruction but along different orientations. e,f) The reconstructed 3D views of the 3% Cs alloyed perovskite crystal grown on the nano-substrate. The atomic displacements within slices through the 3% Cs alloyed and nano-substrated perovskite crystal (transparent objects), whose normal direction is g) along the **Q** direction and h) perpendicular to the **Q** direction.

© 2025 Wiley-VCH GmbH

16136829, 0, Downloaded from https://onlinelibrary.wiley.com/doi/10.1002/smll.202501920 by Bo Chen - Tongji University , Wiley Online Library on [23/06/2025]. See the Terms and Conditions (https://onlinelibrary.wiley.com/terms-and-conditions) on Wiley Online Library for rules of use; OA articles are governed by the applicable Creative Commons License

Table 2. The volume fraction and atomic displacement in specific region of the 3% Cs alloyed perovskite crystal (on flat-substrate).

Region	Volume fraction [%]	Average displacement [Å]	Maximum displacement [Å]
Tensile domain	58.52	0.24	0.72
Compressive domain	41.48	−0.28	−1.43

displacement changes to −0.25 Å. The positive-neutral-negative change is also found in the slice images perpendicular to **Q** direction of the reconstructed $MAPbI_3$ crystal on nano-substrated sample (Figure 4d), but not found in that of the flat-substrated sample (Figure 3a–d). The change of strain from tensile to compressive among the BCDI results demonstrates nanoscale heterogeneity of the strain in the synthesized crystals on the nano-substrate. This may result from the uneven interface between the $MAPbI_3$ film and the nano-substrate. The morphology and size characteristics of the substrates will affect the homogeneity of strain in the thin film.[30] Due to the presence of the nanocolumns on the nano-substrate, the substrate's surface is not flat but curved with multiple undulations, with different morphologies in different nanoregions. The growth of $MAPbI_3$ crystals will be affected by the morphology difference of regions of the substrate. The tensile strain is introduced in the regions with nanocolumns, while no strain could be introduced in the regions without nanocolumns.

The reconstructed 3% Cs alloyed perovskite crystal on the nano-substrate is shown in Figure 4e–h. This measured crystal is a particle with one side protruding and the other side concave (Figure 4e,f). The atomic displacements within the whole crystal are all positive (Figure 4g,h), ranging from 0 to 1.63 Å (Figure S8b, Supporting Information), indicating no deviation of strain to the negative, which suggests the homogeneity of strain within the crystal. The strain heterogeneity could be caused by Cs^+ segregation and unevenness of the nano-substrate surface as discussed above. However, it can be found that when combining both applications of Cs alloying with 3% and providing a nano-substrate, the compressive strain introduced by 3% Cs alloying and the tensile strain introduced by the nano-substrate compensate for each other, resulting in the strain "homogeneity" in the 3% Cs alloyed perovskite crystal grown on the nano-substrate.

2.4. Stability Tests

The XRD patterns of the perovskite films cured in Argon (Ar) atmosphere are shown in **Figure 5**a–f, where the intensities of PbI_2 peaks are found increased after being cured for 30 d. The integral areas of PbI_2 peaks obtained from XRD patterns are shown in Figure 5g. After curing, the integral areas increase, indicating the formations of PbI_2 in perovskite samples. The formations of PbI_2 suggest the decomposition of perovskite films and the decomposition rates were calculated according to the method in the "Calculation of Decomposition Rate" part in the Supporting Information. The mean decomposition rates are shown in Figure 5h. For flat-substrated samples, 3% Cs alloyed perovskite film exhibits a faster decomposition compared with that of non-Cs alloyed perovskite film (Figure 5h). It can be inferred that the nanoscale heterogeneity of strain in 3% Cs alloyed perovskite crystals on flat-substrate (Figure 3e–m) accelerates the decomposition, as the tensile-strained nanoregion would undermine the structural stability. When providing a nano-substrate on 3% Cs alloyed perovskite film, the decomposition rate falls rapidly (Figure 5h). Providing a nano-substrate on 3% Cs alloyed perovskite films can eliminate the nanoscale heterogeneity of strain (Figure 4e–h), resulting in a much slower decomposition. The 7% Cs alloyed perovskite films exhibit the lowest decomposition rate (Figure 5h), indicating the best stability among samples.

Due to the absence of oxygen, humidity, and light illumination, the decomposition can be attributed to the intrinsic instability of perovskite films. Their decomposition into PbI_2 is related to the ion migration, which is highly sensitive to the strain.[31] Specifically, the activation energy (E_a) of ion migration in the perovskite films is significantly reduced under tensile strain, resulting in the acceleration of ion migration.[14] The accelerated ion migration is responsible for the faster decomposition of perovskite films into PbI_2, because MA^+ and I^- ions would migrate more easily from $MAPbI_3$ lattice sites, producing PbI_2. Moreover, tensile strain can decrease the formation energy of halide ion vacancies, providing channels for ion migration.[10,32] Compressive strain, on the other hand, can decrease both the activation energy of ion migration and the formation energy of halide ion vacancies. Thus, the ion migration and the subsequent decomposition are suppressed under compressive strain. After 3% Cs alloying, the introduction of compressive strain is expected to enhance the stability.[33] However, averagely compressive strain of −0.07% (Figure 2a) is too low to effectively improve the stability. At this strain degree, the nanoscale heterogeneity/homogeneity of strain has a more significant effect on the structural stability (Figure 5h). The influence of the tensile-strained region on the stability of perovskite films at low average strain degree cannot be ignored. In these regions, the tensile strain provides additional driving force for ion migration and promotes the formation of ion vacancies. The accelerated ion migration facilitates the disruption of the $[PbI_6]^{4-}$ framework and the decomposition into PbI_2, resulting in the decreased stability of the perovskite films. In homogeneously strained perovskite films, the tensile strain is lacking. The compressive strain decelerates ion migration in perovskite films, improving their intrinsic stability. After 7% Cs alloying, the averagely compressive strain in perovskite films reach to relatively high absolute values (−0.99% for flat-substrated samples and −1.19% for nano-substrated samples) (Figure 2a). At this strain degree, average strain can suppress the detrimental impacts of strain heterogeneity and starts to play a dominant role for influencing the stability. Due to the relatively large degree of compressive strain, the adverse effect of tensile strain on ion migration is offset. Since the ion migration in the perovskite films is inhibited by compressive strain, both the phase separation and decomposition caused by vacancy defects are suppressed. The compressive strain can compact the lattice, enhancing

© 2025 Wiley-VCH GmbH

16136829, 0, Downloaded from https://onlinelibrary.wiley.com/doi/10.1002/smll.202501920 by Bo Chen - Tongji University , Wiley Online Library on [23/06/2025]. See the Terms and Conditions (https://onlinelibrary.wiley.com/terms-and-conditions) on Wiley Online Library for rules of use; OA articles are governed by the applicable Creative Commons License

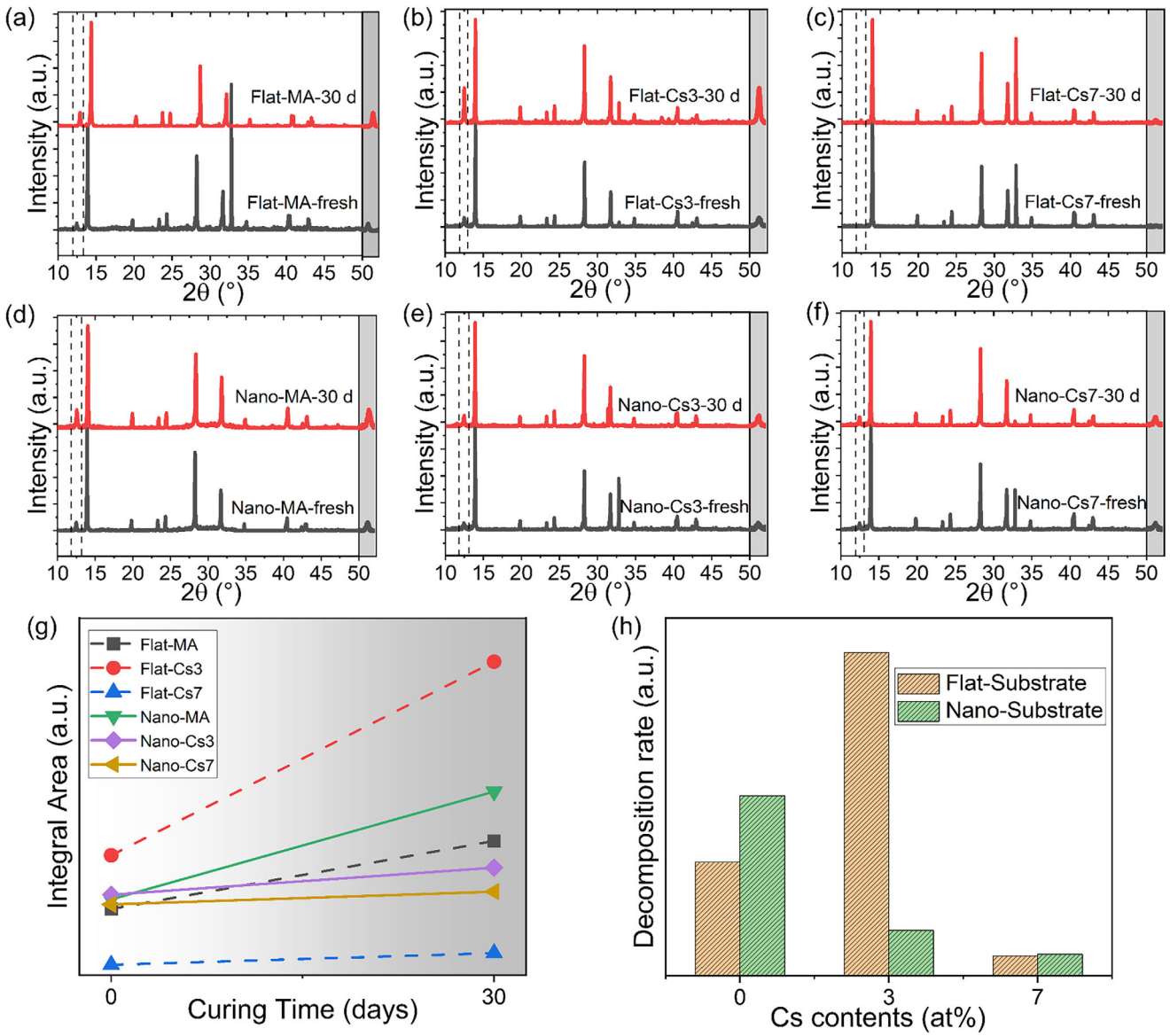

Figure 5. The stability and properties of the perovskite films. The XRD patterns and the zoomed-in views of the dashed areas (gray areas on the right of each panel) of the perovskite films prepared on flat-substrates cured for different times (fresh and 30 d) when the Cs content is a) 0, b) 3 at%, and c) 7 at%. The XRD patterns and the zoomed-in views of the dashed areas (gray areas on the right of each panel) of the perovskite films prepared on nano-substrates cured for different times (fresh and 30 d) when the Cs content is d) 0, e) 3 at%, and f) 7 at%. g) The integral areas of PbI_2 peaks in the XRD patterns of perovskite films with different curing times. h) The decomposition rates of different perovskite films.

structural stability and suppressing the decomposition into PbI_2.[34] In addition to enhancing the intrinsic stability, Cs alloying is found to enhance the resistance of perovskite films against moisture and oxygen, preventing their decomposition to hydrates (Figure S9, Supporting Information).

The FTIR spectra of perovskite films are shown in **Figure 6a**. After Cs alloying and providing nano-substrates, the locations of the infrared absorption peaks remain unchanged, indicating the remaining functional groups and the lengths and angles of the chemical bonds (Figure 6a). Specifically, the peaks observed at 3185 and 2957 cm^{-1} can be assigned to N—H stretching and C—H stretching, respectively. The peaks at 1580 and 1462 cm^{-1} can be assigned to NH_3 asymmetric bending and NH_3 symmetric bending, respectively. The peaks at 1105, 1018, and 904 cm^{-1} can be assigned to symmetric C—N stretching, C—N stretching and CH_3—NH_3 rocking, respectively. These peaks are consistent with the previous reports,[35] suggesting the vibration of MA^+ ions in the perovskite films. After Cs alloying from 0% to 7%, the intensities of the peaks of MA^+ enhance (see the insert of Figure 6a), suggesting the enhanced absorption intensity with the introduction of compressive strain. The MA^+ ions in the nonstrained perovskite films rotate freely, and the variations of dipole moments in all directions cancel each other out. After Cs alloying, the introduced compressive strain would cause the impact arrangement of $[PbI_6]^{4-}$ octahedra, thus the MA^+ ions are compressed and orderly orientated.[36] The ordering orientations of MA^+ lead to the

© 2025 Wiley-VCH GmbH

16136829, 0, Downloaded from https://onlinelibrary.wiley.com/doi/10.1002/smll.202501920 by Bo Chen - Tongji University , Wiley Online Library on [23/06/2025]. See the Terms and Conditions (https://onlinelibrary.wiley.com/terms-and-conditions) on Wiley Online Library for rules of use; OA articles are governed by the applicable Creative Commons License

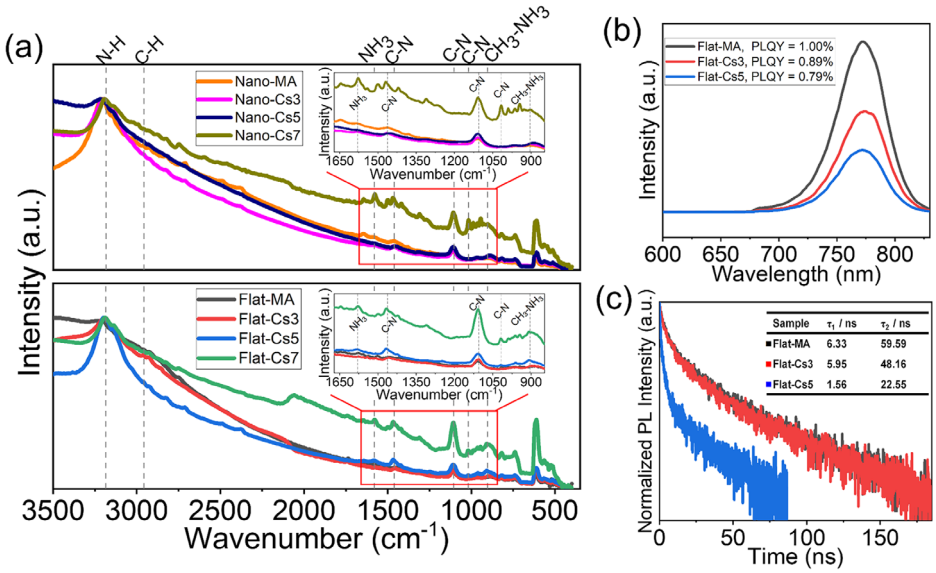

Figure 6. The optical spectra of the perovskite films. a) The Fourier transform infrared (FTIR) spectra of the perovskite films. The inserts are the zoomed-in views of the parts in the red boxes. b) The PL spectra and the photoluminescence quantum yield (PLQY) results of the perovskite films. c) The time-resolved photoluminescence spectroscopy (TRPL) spectra and the fitted PL lifetimes of the perovskite films. The inserted table lists the fitted τ_1 and τ_2 values of the TRPL decays.

same direction of variation of the dipole moments. As a result, the pronounced net dipole moment variation enhances the infrared absorption intensity.

The photoluminescence (PL) was performed to investigate the nonradiative recombination of charged carriers, which is adverse in the operation of perovskite device.[37] After 3% Cs alloying, the intensity of PL peak of the perovskite film decreases compared with that of the non-Cs alloyed $MAPbI_3$ film (Figure 6b). The decrease of the PL peak indicates the increasing nonradiative recombination of the carriers in the semiconductor materials, which is caused by the increasing trap density.[38] After 3% Cs alloying, due to the strain heterogeneity, the tensile strain regions in the perovskite films accelerate ion migration and promote the formation of the defects. The increased defect density would cause the increased trap density and the enhanced nonradiative recombination, resulting in the PL quenching. When the Cs content increases from 3% to 5%, the PL intensity reduces, which indicates further increased trap density (Figure 6b). The increased trap density in 5% Cs alloyed perovskite films may originate from the Cs segregation, which causes the strain heterogeneity and would introduce extra traps to capture the carriers. The photoluminescence quantum yield (PLQY) measurement results are shown in Figure 6b. As the Cs content increases from 0% to 5%, the PLQY of the perovskite films decreases from 1.00% (non-Cs alloying) to 0.89% (3% Cs alloying) to 0.79% (5% Cs alloying). The continuously decreased PLQY validates that the heterogeneous strain promotes defect formation and thus enhances defect-induced nonradiative recombination.[39]The time-resolved photoluminescence spectroscopy (TRPL) was conducted to verify the increased trap density and the results are shown in Figure 6c. The double-exponential fitting function was used to fit the TRPL decays:

$$I = A_1 e^{(-t/\tau_1)} + A_2 e^{(-t/\tau_2)} \quad (2)$$

where I is the PL intensity, A_1 and A_2 are corresponding coefficients, t is time, and τ_1 and τ_2 are PL lifetimes, respectively. τ_1 (shorter lifetime) is assigned to charge carriers trapping into nonradiative trap states, while τ_2 (longer lifetime) is assigned to radiative recombination.[40] After 3% Cs alloying, τ_1 of the perovskite films decreased from 6.33 to 5.95 ns (see inserted table in Figure 6c), which indicates the increased trap density. After 3% Cs alloying, the strain is not homogeneous and the impact of the tensile strain cannot be ignored. The defect density in the tensile domain increases due to the lower formation energy of defects, such as MA^+ and I^- vacancies. These increased defects would serve as the nonradiative centers to capture charge carriers, which results in the enhanced nonradiative recombination of carriers and the decrease of their lifetime.[41] While Cs content increases from 3% to 5%, τ_1 further decreases from 5.95 to 1.56 ns, possibly due to the higher Cs content causing the Cs segregation and enhancing the strain heterogeneity. As a result, the enhanced strain heterogeneity in 5% Cs alloyed perovskite films leads to the increase in the trap density and the nonradiative recombination rate. The bandgap of perovskite films after 5% Cs alloying remains unchanged (Figure S10, Supporting Information).

3. Conclusions

Controllable regulation of strain in $MAPbI_3$ crystals was achieved by using Cs alloying and by providing nano-substrates. Cs alloying can introduce compressive strain to the $MAPbI_3$ films with a maximum of −1.19% (averagely) in 7% Cs alloyed perovskite films in this study. This is due to the smaller size of Cs^+ occupying the A site in the $MAPbI_3$ lattice. The lattice contraction results in compressive strain. On the other hand, providing nano-substrates can introduce tensile strain to the non-Cs alloyed $MAPbI_3$ films with 0.27% (averagely) in this study. This could

© 2025 Wiley-VCH GmbH

16136829, 0, Downloaded from https://onlinelibrary.wiley.com/doi/10.1002/smll.202501920 by Bo Chen - Tongji University , Wiley Online Library on [23/06/2025]. See the Terms and Conditions (https://onlinelibrary.wiley.com/terms-and-conditions) on Wiley Online Library for rules of use; OA articles are governed by the applicable Creative Commons License

be caused by the nanocolumns on the nano-substrates increasing the constraint on the nucleation and growth of the $MAPbI_3$ crystals.

The homogeneity/heterogeneity of strain in different perovskite films at nanoscale was revealed by using BCDI measurements on the selected crystals. The pristine $MAPbI_3$ crystal without Cs alloying on the flat-substrate exhibits good homogeneity of strain distribution. Through 3% Cs alloying, the strain homogeneity is destroyed, as the strain starts to vary from tensile to compressive, and both kinds of domains were found in the crystals. This heterogeneity of strain should be the result of Cs segregation. The nano-substrate application can also cause heterogeneity of strain in the perovskite film crystals, as nanostructural difference can influence the nucleation and growth of the $MAPbI_3$ crystals. At low strain degree (−0.07%, absolute value), it was found that the strain heterogeneity accelerates the decomposition and the strain homogeneity inhibits the decomposition. At high strain degree (more than −0.99%, absolute value), compressive strain can significantly enhance the structural stability. Besides these, it was found that the introduced compressive strain via 3–7% Cs alloying could compact MA^+ cations and enhance the dipole moment variation, which results in the enhanced infrared absorption capabilities. It was found that the strain heterogeneity would increase the trap density and enhance the nonradiative recombination of the carriers. The findings in this study improve our understanding of strain engineering and application of PSCs in the future.

Currently, the nonuniform distribution of strain in perovskite films has attracted great attention of the researchers. Future research could focus on the dynamic evolution and regulation of the strain fields in perovskite materials. Thanks to the upgrades to the diffraction-limited synchrotron sources and the application of the machine learning techniques, fast data acquisition and complex reconstruction are available for BCDI measurements, which allows the researchers to investigate the material kinetics at the nanoscale, such as the real-time dynamic strain evolution in perovskite materials under operational conditions. Besides, the higher temporal resolution would allow the study of the rapid reaction processes of materials, such as the rapid charging/discharging of battery materials and the phase transition of photoelectric materials.

4. Experimental Section

Preparations of $MAPbI_3$ Films: The precursor solutions were obtained by mixing $MAPbI_3$ and $CsPbI_3$ in predetermined molar ratios, using a solvent mixture of dimethyl sulfoxide (DMSO) and dimethylformamide (DMF) with a volume ratio of DMSO: DMF = 4: 1. The 1 M precursor solutions were stirred for 5 h until completely dissolved. The single crystal Si wafers (diameter = 100 mm, single-sided polished) were purchased from Suzhou Crystal Silicon Electronic and Technology Co, Ltd, China. The doping type is P-type doping (Boron doping) and the orientation is (100). The Si wafers used in the process were categorized as follows: untreated ones were called as flat-substrates, while those etched to feature nanocolumns on their surfaces were called as nano-substrates. Both types of substrates underwent a cleaning regimen that included DMSO, deionized water, and a 5-min oxygen plasma treatment. The perovskite films were prepared in a glove box filled with an argon (Ar) atmosphere. The process began with dropping 30 µL precursor solution onto each substrate, followed by a meticulous two-step spin-coating procedure (1000 rpm for 3 s and 2850 rpm for 45 s). Toluene was added 30 s before the end of spin coating. After spin coating, the intermediate phase films were annealed at 100 °C for 10 min to obtain the perovskite films. The films on flat-substrates were named as Flat-MA (for those without Cs alloying) and Flat-Csx, where *x* denotes the molar percentage of Cs ($x = 1, 3, 5, 7$). Correspondingly, films on nano-substrates were named as Nano-MA (Cs-free) and Nano-Csx. A list of sample names can be found in **Table 3**.

Table 3. The names of the samples.

Samples of different cationic configurations and substrates	Name
$MAPbI_3$ on flat-substrate	Flat-MA
$Cs_{0.01}MA_{0.99}PbI_3$ on flat-substrate	Flat-Cs1
$Cs_{0.03}MA_{0.97}PbI_3$ on flat-substrate	Flat-Cs3
$Cs_{0.05}MA_{0.95}PbI_3$ on flat-substrate	Flat-Cs5
$Cs_{0.07}MA_{0.93}PbI_3$ on flat-substrate	Flat-Cs7
$MAPbI_3$ on nano-substrate	Nano-MA
$Cs_{0.01}MA_{0.99}PbI_3$ on nano-substrate	Nano-Cs1
$Cs_{0.03}MA_{0.97}PbI_3$ on nano-substrate	Nano-Cs3
$Cs_{0.05}MA_{0.95}PbI_3$ on nano-substrate	Nano-Cs5
$Cs_{0.07}MA_{0.93}PbI_3$ on nano-substrate	Nano-Cs7

Laboratory X-Ray and Electron Characterization: The XRD patterns were recorded by a Brucker D8 Advance diffractometer, with 40 kV voltage and 40 mA working current. The scanning range of 2θ is 10°–50°, with step of 2° and speed of 2° min^{-1}. The SEM images were obtained by a Zeiss Sigma 300 VP machine with 3 kV voltage. The elemental analysis was carried out by an EDS, Oxford X-MAX. The newly synthesized perovskite films were placed in the glove box with Ar atmosphere at room temperature for 30 d without exposure to light, oxygen, or moisture. The new and the stored perovskite film samples were measured by XRD once they reached the specific target storing time.

BCDI Measurements: BCDI measurements were carried out at the I13-1 beamline of the Diamond Light Source (UK) using X-rays with energy of 9 keV. The diffraction patterns were recorded using an Excalibur X-ray photon-counting detector, which was placed at a distance of 2.81 m from the sample. The 2θ during BCDI measurement is set to 12.5°, which corresponds to the (110) Bragg reflection of $MAPbI_3$ crystals according to the XRD measurement. The samples were rotated with a step of 0.01° around the Bragg peak within a range of 0.40° to collect the slices of diffraction patterns to cover the full 3D diffraction patterns in reciprocal space.

An iterative algorithm with error reduction and hybrid input—output steps was used for reconstructions.[42] The iterations were performed back and forth between the diffraction patterns (in reciprocal space) and crystal electron density (in real space). During each iteration, a support was applied to the results in real space. The shrink-wrap method was used to update the support during the iterations.[43] 300 iterations were used for phase retrieval, in which full convergence of a chi-square error metric was reached and the reconstruction was found to be reproducible from different random starts.

Spectral Characterization: FTIR spectra were acquired using a Brucker Tensor II spectrometer, with the testing wavenumber ranging from 5998 to 400 cm^{-1}. UV–vis spectra were recorded using an Agilent Cary 60 spectrometer. PL and TRPL were recorded using FLS 1000 photoluminescence spectrometer, in which the excitation wavelength is 468 nm, with a step of 1 nm and a dwell time of 0.1 s. PLQY was calculated using the integration sphere.

Supporting Information

Supporting Information is available from the Wiley Online Library or from the author.

© 2025 Wiley-VCH GmbH

16136829, 0, Downloaded from https://onlinelibrary.wiley.com/doi/10.1002/smll.202501920 by Bo Chen - Tongji University , Wiley Online Library on [23/06/2025]. See the Terms and Conditions (https://onlinelibrary.wiley.com/terms-and-conditions) on Wiley Online Library for rules of use; OA articles are governed by the applicable Creative Commons License

Acknowledgements

This work was supported by the Fundamental Research Funds for the Central Universities (Tongji University) with Grant Nos. 22120210516 and 2023-2-ZD-05. The BCDI experiments were carried out at the beamline I13-1 at the Diamond Light Source, UK. Work at University College London (UCL) was supported by Engineering and Physical Sciences Research Council (EPSRC), UK.

Conflict of Interest

The authors declare no conflict of interest.

Data Availability Statement

All the data supporting the findings of this work are presented in the main text or the supporting information. The related data are available from the correspondence authors upon reasonable requests.

Keywords

3D nanoscale strain mapping, bragg coherent X-ray diffraction imaging (BCDI), long-term stability, perovskite films

Received: February 14, 2025
Revised: May 30, 2025
Published online:

[1] Z. Li, Y. Zhao, X. Wang, Y. Sun, Z. Zhao, Y. Li, H. Zhou, Q. Chen, *Joule* **2018**, *2*, 1559.
[2] H. Zhang, X. Zhang, C. Liu, S.-T. Lee, J. Jie, *ACS Nano* **2016**, *10*, 5113.
[3] Y.-H. Kim, S. Kim, A. Kakekhani, J. Park, J. Park, Y.-H. Lee, H. Xu, S. Nagane, R. B. Wexler, D.-H. Kim, S. H. Jo, L. Martínez-Sarti, P. Tan, A. Sadhanala, G.-S. Park, Y.-W. Kim, B. Hu, H. J. Bolink, S. Yoo, R. H. Friend, A. M. Rappe, T.-W. Lee, *Nat. Photonics* **2021**, *15*, 148.
[4] a) Y. Yang, M. T. Hoang, D. Yao, N. D. Pham, V. T. Tiong, X. Wang, W. Sun, H. Wang, *Sol. Energy Mater. Sol. Cells* **2020**, *210*, 110517; b) G. Tong, D.-Y. Son, L. K. Ono, H.-B. Kang, S. He, L. Qiu, H. Zhang, Y. Liu, J. Hieulle, Y. Qi, *Nano Energy* **2021**, *87*, 106152.
[5] A. Kojima, K. Teshima, Y. Shirai, T. Miyasaka, *J. Am. Chem. Soc.* **2009**, *131*, 6050.
[6] NREL, *Best Research-Cell Efficiency Chart*, US Department of Energy, Washington DC **2019**.
[7] a) N. De Marco, H. Zhou, Q. Chen, P. Sun, Z. Liu, L. Meng, E.-P. Yao, Y. Liu, A. Schiffer, Y. Yang, *Nano Lett.* **2016**, *16*, 1009; b) Y. Lei, Y. Li, C. Lu, Q. Yan, Y. Wu, F. Babbe, H. Gong, S. Zhang, J. Zhou, R. Wang, R. Zhang, Y. Chen, H. Tsai, Y. Gu, H. Hu, Y.-H. Lo, W. Nie, T. Lee, J. Luo, K. Yang, K.-I. Jang, S. Xu, *Nature* **2022**, *608*, 317.
[8] a) S. Xiang, Z. Fu, W. Li, Y. Wei, J. Liu, H. Liu, L. Zhu, R. Zhang, H. Chen, *ACS Energy Lett.* **2018**, *3*, 1824; b) A. Walsh, S. D. Stranks, *ACS Energy Lett.* **2018**, *3*, 1983.
[9] a) A. N. Beecher, O. E. Semonin, J. M. Skelton, J. M. Frost, M. W. Terban, H. Zhai, A. Alatas, J. S. Owen, A. Walsh, S. J. L. Billinge, *ACS Energy Lett.* **2016**, *1*, 880; b) D. Liu, D. Luo, A. N. Iqbal, K. W. P. Orr, T. A. S. Doherty, Z.-H. Lu, S. D. Stranks, W. Zhang, *Nat. Mater.* **2021**, *20*, 1337.
[10] D.-J. Xue, Y. Hou, S.-C. Liu, M. Wei, B. Chen, Z. Huang, Z. Li, B. Sun, A. H. Proppe, Y. Dong, M. I. Saidaminov, S. O. Kelley, J.-S. Hu, E. H. Sargent, *Nat. Commun.* **2020**, *11*, 1514.
[11] a) N. Rolston, K. A. Bush, A. D. Printz, A. Gold-Parker, Y. Ding, M. F. Toney, M. D. McGehee, R. H. Dauskardt, *Adv. Energy Mater.* **2018**, *8*, 1802139; b) C. Shi, Q. Song, H. Wang, S. Ma, C. Wang, X. Zhang, J. Dou, T. Song, P. Chen, H. Zhou, Y. Chen, C. Zhu, Y. Bai, Q. Chen, *Adv. Funct. Mater.* **2022**, *32*, 2201193; c) T. W. Jones, A. Osherov, M. Alsari, M. Sponseller, B. C. Duck, Y.-K. Jung, C. Settens, F. Niroui, R. Brenes, C. V. Stan, Y. Li, M. Abdi-Jalebi, N. Tamura, J. E. Macdonald, M. Burghammer, R. H. Friend, V. Bulović, A. Walsh, G. J. Wilson, S. Lilliu, S. D. Stranks, *Energy Environ. Sci.* **2019**, *12*, 596; d) B. Li, B. Hou, G. A. J. Amaratunga, *InfoMat* **2021**, *3*, 445.
[12] a) S. Wang, J. Hu, A. Wang, Y. Cui, B. Chen, X. Niu, F. Hao, *J. Energy Chem.* **2022**, *66*, 422; b) W. Lv, Z. Hu, W. Qiu, D. Yan, M. Li, A. Mei, L. Xu, R. Chen, *Adv. Sci.* **2022**, *9*, 2202028.
[13] a) Z. Li, M. Yang, J.-S. Park, S.-H. Wei, J. J. Berry, K. Zhu, *Chem. Mater.* **2016**, *28*, 284; b) H. Wang, C. Zhu, L. Liu, S. Ma, P. Liu, J. Wu, C. Shi, Q. Du, Y. Hao, S. Xiang, H. Chen, P. Chen, Y. Bai, H. Zhou, Y. Li, Q. Chen, *Adv. Mater.* **2019**, *31*, 1904408; c) C. Wu, K. Chen, D. Y. Guo, S. L. Wang, P. G. Li, *RSC Adv.* **2018**, *8*, 2900.
[14] J. Zhao, Y. Deng, H. Wei, X. Zheng, Z. Yu, Y. Shao, J. E. Shield, J. Huang, *Sci. Adv.* **2017**, *3*, aao5616.
[15] B. Yang, D. Bogachuk, J. Suo, L. Wagner, H. Kim, J. Lim, A. Hinsch, G. Boschloo, M. K. Nazeeruddin, A. Hagfeldt, *Chem. Soc. Rev.* **2022**, *51*, 7509.
[16] a) C. Zhu, X. Niu, Y. Fu, N. Li, C. Hu, Y. Chen, X. He, G. Na, P. Liu, H. Zai, Y. Ge, Y. Lu, X. Ke, Y. Bai, S. Yang, P. Chen, Y. Li, M. Sui, L. Zhang, H. Zhou, Q. Chen, *Nat. Commun.* **2019**, *10*, 815; b) B. Chen, J. Song, X. Dai, Y. Liu, P. N. Rudd, X. Hong, J. Huang, *Adv. Mater.* **2019**, *31*, 1902413.
[17] a) I. Robinson, R. Harder, *Nat. Mater.* **2009**, *8*, 291; b) M. A. Pfeifer, G. J. Williams, I. A. Vartanyants, R. Harder, I. K. Robinson, *Nature* **2006**, *442*, 63; c) M. C. Newton, S. J. Leake, R. Harder, I. K. Robinson, *Nat. Mater.* **2010**, *9*, 120.
[18] a) H. N. Chapman, K. A. Nugent, *Nat. Photonics* **2010**, *4*, 833; b) S. Marchesini, *Rev. Sci. Instrum.* **2007**, *78*, 011301.
[19] Y. Liu, P. P. Lopes, W. Cha, R. Harder, J. Maser, E. Maxey, M. J. Highland, N. M. Markovic, S. O. Hruszkewycz, G. B. Stephenson, H. You, *Nano Lett.* **2017**, *17*, 1595.
[20] A. Singer, M. Zhang, S. Hy, D. Cela, C. Fang, T. A. Wynn, B. Qiu, Y. Xia, Z. Liu, A. Ulvestad, N. Hua, J. Wingert, H. Liu, M. Sprung, A. V. Zozulya, E. Maxey, R. Harder, Y. S. Meng, O. G. Shpyrko, *Nat. Energy* **2018**, *3*, 641.
[21] K. W. P. Orr, J. Diao, M. N. Lintangpradipto, D. J. Batey, A. N. Iqbal, S. Kahmann, K. Frohna, M. Dubajic, S. J. Zelewski, A. E. Dearle, T. A. Selby, P. Li, T. A. S. Doherty, S. Hofmann, O. M. Bakr, I. K. Robinson, S. D. Stranks, *Adv. Mater.* **2023**, *35*, 2305549.
[22] J. Xie, Y. Liu, J. Liu, L. Lei, Q. Gao, J. Li, S. Yang, *J. Power Sources* **2015**, *285*, 349.
[23] P. Zaumseil, *J. Appl. Crystallogr.* **2015**, *48*, 528.
[24] Y. Xiong, X. Xu, B. Chen, X. Xu, *Adv. Mater.* **2024**, *36*, 2310427.
[25] V. M. Glazov, A. S. Pashinkin, *High Temp.* **2001**, *39*, 413.
[26] G. P. Nagabhushana, R. Shivaramaiah, A. Navrotsky, *Proc. Natl. Acad. Sci. U. S. A.* **2016**, *113*, 7717.
[27] N. Calisi, S. M. Martinuzzi, A. Giaccherini, M. Innocenti, M. Mannini, F. Carlà, S. Caporali, *Thin Solid Films* **2023**, *783*, 140057.
[28] S.-G. Cao, Y. Li, H.-H. Wu, J. Wang, B. Huang, T.-Y. Zhang, *Nano Lett.* **2017**, *17*, 5148.
[29] T. Kawaguchi, V. Komanicky, V. Latyshev, W. Cha, E. R. Maxey, R. Harder, T. Ichitsubo, H. You, *Nano Lett.* **2021**, *21*, 5945.
[30] Y. Wang, Y. Wei, Z. Zhao, H. Long, Z. Lin, F. Guo, Q. He, C.-X. Huang, Y. Zhu, *Int. J. Plast.* **2021**, *149*, 103159.
[31] X. Sun, P. Shi, J. Shen, J. Shen, L. Tian, J. Xu, Q. Liu, Y. Tian, D. Jin, X. Miao, J. Xue, R. Wang, *Matter* **2025**, *8*, 101920.
[32] D. W. Ferdani, S. R. Pering, D. Ghosh, P. Kubiak, A. B. Walker, S. E. Lewis, A. L. Johnson, P. J. Baker, M. S. Islam, P. J. Cameron, *Energy Environ. Sci.* **2019**, *12*, 2264.

© 2025 Wiley-VCH GmbH

16136829, 0, Downloaded from https://onlinelibrary.wiley.com/doi/10.1002/smll.202501920 by Bo Chen - Tongji University , Wiley Online Library on [23/06/2025]. See the Terms and Conditions (https://onlinelibrary.wiley.com/terms-and-conditions) on Wiley Online Library for rules of use; OA articles are governed by the applicable Creative Commons License

[33] S.-Y. Ju, W. I. Lee, H.-S. Kim, *ACS Appl. Mater. Interfaces* **2022**, *14*, 39996.
[34] S. Wang, A. A. Yousefi Amin, L. Wu, M. Cao, Q. Zhang, T. Ameri, *Small Struct.* **2021**, *2*, 2000124.
[35] a) L. Wang, K. Wang, B. Zou, *J. Phys. Chem. Lett.* **2016**, *7*, 2556; b) A. K. Soopy, S. Liu, A. Najar, *Nanomaterials* **2024**, *14*, 1068; c) M. A. Pérez-Osorio, R. L. Milot, M. R. Filip, J. B. Patel, L. M. Herz, M. B. Johnston, F. Giustino, *J. Phys. Chem. C* **2015**, *119*, 25703.
[36] L. Zhang, W. Geng, C.-J. Tong, X. Chen, T. Cao, M. Chen, *Sci. Rep.* **2018**, *8*, 7760.
[37] S. D. Stranks, H. J. Snaith, *Nat. Nanotechnol.* **2015**, *10*, 391.
[38] X. Zang, S. Xiong, S. Jiang, D. Li, H. Wu, H. Ren, A. Cao, B. Li, Z. Ma, J. Chen, L. Ding, J. Tang, Z. Sun, J. Chu, Q. Bao, *Adv. Mater.* **2024**, *36*, 2309991.
[39] C. Shi, J. Wang, X. Lei, Q. Zhou, W. Wang, Z. Yang, S. Liu, J. Zhang, H. Zhu, R. Chen, Y. Pan, Z. Tan, W. Liu, Z. Zhao, Z. Cai, X. Qin, Z. Zhao, J. Li, Z. Liu, W. Chen, *Nat. Commun.* **2025**, *16*, 3029.
[40] T. Du, J. Kim, J. Ngiam, S. Xu, P. R. F. Barnes, J. R. Durrant, M. A. McLachlan, *Adv. Funct. Mater.* **2018**, *28*, 1801808.
[41] S. Xiong, X. Zang, H. Wu, D. Li, S. Jiang, L. Ding, B. Li, M. Fahlman, Q. Bao, *Nano Energy* **2025**, *134*, 110538.
[42] J. R. Fienup, *Appl. Opt.* **1982**, *21*, 2758.
[43] S. Marchesini, H. He, H. N. Chapman, S. P. Hau-Riege, A. Noy, M. R. Howells, U. Weierstall, J. C. H. Spence, *Phys. Rev. B* **2003**, *68*, 140101.

© 2025 Wiley-VCH GmbH

16136829, 0, Downloaded from https://onlinelibrary.wiley.com/doi/10.1002/smll.202501920 by Bo Chen - Tongji University , Wiley Online Library on [23/06/2025]. See the Terms and Conditions (https://onlinelibrary.wiley.com/terms-and-conditions) on Wiley Online Library for rules of use; OA articles are governed by the applicable Creative Commons License